NASA TECHNICAL NOTE

NASA TN D-3024

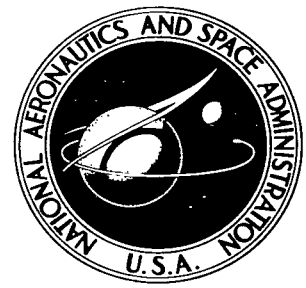

NASA TN D-3024

DESIGN AND OVERALL PERFORMANCE OF AN AXIAL-FLOW PUMP ROTOR WITH A BLADE-TIP DIFFUSION FACTOR OF 0.66

by Max J. Miller and James E. Crouse

Lewis Research Center
Cleveland, Ohio

NATIONAL AERONAUTICS AND SPACE ADMINISTRATION • WASHINGTON, D. C. • SEPTEMBER 1965

DESIGN AND OVERALL PERFORMANCE OF AN AXIAL-FLOW PUMP ROTOR WITH A BLADE-TIP DIFFUSION FACTOR OF 0.66

By Max J. Miller and James E. Crouse

Lewis Research Center
Cleveland, Ohio

NATIONAL AERONAUTICS AND SPACE ADMINISTRATION

For sale by the Clearinghouse for Federal Scientific and Technical Information
Springfield, Virginia 22151 – Price $2.00

DESIGN AND OVERALL PERFORMANCE OF AN AXIAL-FLOW PUMP ROTOR WITH A BLADE-TIP DIFFUSION FACTOR OF 0.66

by Max J. Miller and James E. Crouse

Lewis Research Center

SUMMARY

A 9-inch-diameter axial-flow pump rotor with an 0.8 hub-tip radius ratio and a blade-tip diffusion factor of 0.66 was designed by blade-element techniques and tested in water. With this level of loading, a relatively high flow coefficient and a radial distribution of energy addition increasing from hub to tip were required. These design conditions were required to obtain a head-rise coefficient approximately constant radially and a gradient of outlet flow coefficient which was considered acceptable. A flow coefficient φ_i of 0.466 was selected.

At design flow, the rotor produced an overall head-rise coefficient of 0.391 as compared to the design value of 0.427. Design efficiency was 92.8 percent while an overall efficiency of 95.5 percent was achieved experimentally. As flow was reduced, the rotor operated in a stalled condition at flow coefficients below $\varphi = 0.380$. Static pressure fluctuations increased by a factor of 20 to 30 at the inlet and by a factor of approximately 4 at the outlet when the rotor stalled.

At the design flow, a decrease in head-rise coefficient due to cavitation occurred at a net positive suction head H_{sv} of 115 feet (blade cavitation number $\overline{k} = 0.27$). As H_{sv} was decreased from a noncavitating value, for $0.38 < \overline{\varphi} < 0.54$, a slight improvement in head rise was indicated just prior to a fall off in performance.

INTRODUCTION

When selecting a pump for application in a particular rocket propulsion system, the high specific speed axial-flow pump offers advantages in certain areas. Axial-flow pumps are easy to stage, the number of stages in an existing design can be increased without large mechanical changes, and a blade-element design system can be used. The weight of a pump of this type is minimized when a minimum number of stages is utilized

to produce a given pressure rise. One method of reducing the number of stages is to raise individual blade loading to a limiting value. A study is being conducted at the Lewis Research Center to determine maximum blade loadings that can be realized in a single-stage axial-flow rotor. The level of blade loading must be consistent with acceptable values of efficiency, stall margin, and stable operating flow range.

The stages which compose the main pressure producing portion of a multistage axial-flow pump characteristically have airfoil sections, relatively short chords, and high hub-tip radius ratios. The hydrodynamic design of these stages is governed primarily by blade-loading considerations.

In the following discussion a measure of the blade loading is provided by a blade diffusion factor, or D-factor, which is developed in reference 1. The D-factor reflects the blade-suction surface velocity gradients and is computed from blade inlet and outlet velocity diagrams. The initial levels of blade loading chosen for a typical loaded axial-flow pump rotor were the levels where losses began to increase rapidly with increased loading (ref. 2) for inlet stage axial-flow compressor rotors. These levels occurred at D-factors of approximately 0.4 in a rotor tip region and approximately 0.6 at all other radial stations. A tip D-factor of 0.43 was applied to the design of a 0.7 hub-tip ratio, single-stage-pump rotor whose design and performance are reported in references 3 and 4. Analysis of the performance of this rotor indicated that the levels of loading could be further increased.

The study of blade loading limits was extended by the design, fabrication, and testing of an 0.8 hub-tip ratio, axial-flow rotor with a blade-tip D-factor of 0.66. This report presents the design and overall performance of the latter rotor at both cavitating and noncavitating flow conditions. The variation of head rise across the blade at midpassage as flow was reduced through the blade-stall region and toward shutoff is also presented.

PUMP DESIGN

General Characteristics

The design system used for this rotor assumed blade-element flow and axial symmetry. Using a blade-element flow, both the velocity diagram calculations and the blade-section profile designs were conducted across a number of surfaces of revolution. In this design, blade elements were assumed to lie along cylindrical surfaces and were stacked on a radial line through the centers of gravity of the individual sections.

A velocity diagram study which assumed no inlet whirl and no change in axial velocity across the rotor indicated that, for a given level of blade loading (D-factor), the ideal head-rise coefficient was increased as the inlet flow coefficient was increased. Some of

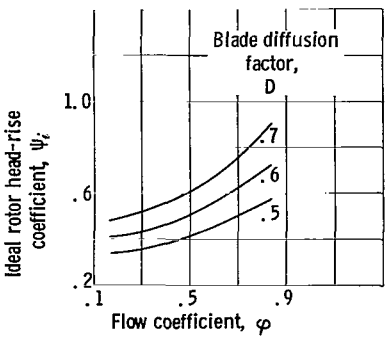

Figure 1. - The variation of ideal head-rise coefficient assuming no inlet whirl and no change in axial velocity across the rotor.

the results of this study are shown in figure 1 to demonstrate the desirability of increasing the flow coefficient at the inlet to highly loaded stages.

However, in a multistage application some limitations on the level of flow coefficient are introduced by the inducer which, typically, has a low inlet flow coefficient and a low hub-tip ratio. The higher flow coefficient for the loaded stages must be obtained by contracting the flow passage, which results in high hub-tip ratios for the loaded stages. Thus, for very high flow coefficients the blades of a loaded stage may be quite short.

With these limitations in mind the radius ratio of 0.8 was selected for this rotor. A rotor with a 9-inch tip diameter was chosen for compatibility with existing rig components. These choices resulted in a blade height of 0.9 inch which was considered satisfactory for measuring blade-element performance data.

Velocity Diagrams

The inlet velocity diagrams were computed from a selected ideal flow coefficient φ_i and the assumptions of a radially constant, axial inlet velocity with no prewhirl. The axial velocity used to compute φ_i was based on the total flow rate and the inlet geometric area. (All symbols are defined in appendix A.)

A number of conditions were imposed on the computation of outlet velocity diagrams. First, the rotor was to produce a total head rise approximately constant radially. Because the inlet total head was assumed constant radially, this design condition tended to minimize any mixing losses and tended toward reducing radial gradients of axial velocity thus facilitating staging. Secondly, the level of blade loading was raised above that used in current practice by requiring a tip D-factor in the range of 0.65 to 0.70. Finally, the losses incurred in the flow across each element were to be related to blade loading, or D-factor.

The procedure used to achieve these required outlet conditions is given in the following eight steps. The equations utilized in the calculation procedure are presented in appendix B. The steps in the procedure were:

1. A radial distribution of ψ_i (ideal energy addition) was selected taking into consideration the anticipated radial distribution of loss.

2. Next an outlet flow coefficient φ_2 distribution (radially constant) was assumed, and outlet velocity diagrams were computed at five radial locations.

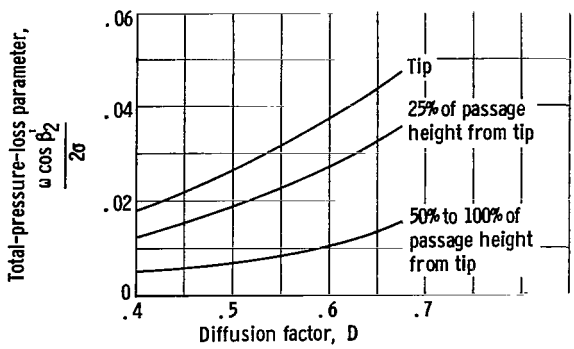

Figure 2. - Preliminary curves of total-pressure-loss parameter against diffusion factor.

3. D-factor values were computed from the inlet velocity diagrams and the outlet velocity diagrams of step 2.

4. Blade loading was related to loss through the use of preliminary curves of the total-pressure-loss parameter, $\frac{\overline{\omega}\cos\beta_2'}{2\sigma}$ against D-factor (fig. 2) similar to those presented in reference 2. The different curves in figure 2 were used for the five radial locations to account for the effects of blade-tip clearance, secondary flows, and other radially varying losses. Because the curves shown in figure 2 depended primarily on performance data from two high-staggered blade rows, caution should be exercised in applying the values generally.

5. The selected values of ψ_i and the computed loss were used in a radial equilibrium expression to compute a new distribution of φ_2. This new distribution φ_2 was required to satisfy both radial equilibrium and continuity. In this calculation, an initial value of φ_2 was assumed at one radial location and the radial gradient of φ_2 required to satisfy radial equilibrium was then computed. This radial distribution of φ_2 was then integrated over the flow passage to check continuity. A new value of φ_2 was assumed and the computations were repeated until a distribution of φ_2 was found that satisfied both radial equilibrium and continuity.

6. The final φ_2 distribution computed in step 5 was used to repeat steps 2 to 5. This process was repeated until the φ_2 distribution computed in step 5 compared with that assumed in step 2 within an acceptable limit. The iteration converged rapidly.

7. The rotor-head-rise coefficient ψ was computed from ψ_i, the inlet velocity diagram, and the loss coefficient $\overline{\omega}$ found in step 4.

8. Next, the radial distributions of ψ and φ_2 were examined to see if large gradients existed. If necessary, changes in φ_i or the distribution of ψ_i were made to reduce the gradients to a level considered acceptable.

The effects of varying φ_i and radial distribution of ψ_i in a design of this type are demonstrated by the three examples presented in figure 3. A ψ_i varying linearly from 0.5 at the tip to 0.4 at the hub and a φ_i of 0.36 were used in the first example (fig. 3(a)). Continuity had not yet been satisfied when φ_2 went to zero at the tip in this example. This was not considered an acceptable gradient.

The effects of increasing φ_i to 0.466 and of changing ψ_i to a radially constant value of 0.45 are shown in the second example (fig. 3(b)). Both the resulting ψ and φ_2 gradients in the tip region were larger than desired.

The third example shows the distributions resulting from a $\varphi_i = 0.466$ and a ψ_i

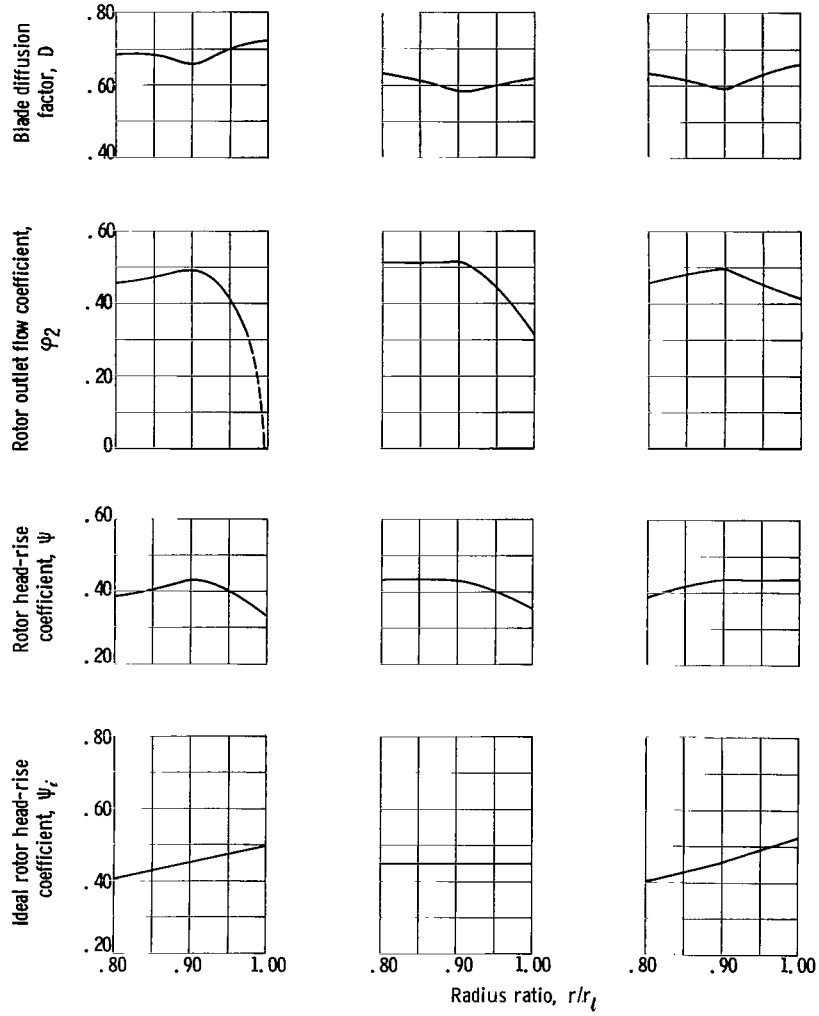

(a) Ideal flow coefficient, 0.36.

(b) Ideal flow coefficient, 0.466.

(c) Ideal flow coefficient, 0.466.

Figure 3. - Selected radial distributions for three combinations of ideal head-rise coefficient and flow coefficient values.

TABLE I. - VELOCITY DIAGRAM DESIGN VALUES

Radius ratio, r/r_t	Outlet flow coefficient, φ_2	Relative inlet flow angle, β_1', deg	Change in relative flow angle, $\Delta\beta'$, deg	Rotor head-rise coefficient, ψ	Loss coefficient, $\overline{\omega}$	Blade diffusion factor, D
1.00	0.415	65.0	16.0	0.438	0.1396	0.664
.95	.457	63.9	20.2	.437	.0906	.632
.90	.499	62.6	24.2	.439	.0291	.595
.85	.479	61.3	25.5	.414	.0319	.614
.80	.454	59.8	26.7	.387	.0364	.631

varying linearly from 0.523 at the tip to 0.454 at midpassage and from 0.454 at midpassage to 0.403 at the hub (fig. 3(c)). The resulting distributions of ψ and φ_2 were considered satisfactory.

The plots shown in figures 3(a) and (c) illustrate the desirability of using a high φ_i for this rotor design. It shows that the increased energy in the outlet axial velocity allowed radial equilibrium requirements to be met without a large gradient of outlet axial velocity.

Velocity diagram parameters computed for the design of this rotor are summarized in table I.

Blade Design

After the fluid velocity diagrams are established, a blade must be designed to produce the required flow angles. A double-circular arc blade was chosen as the basic blade shape. Pressure and suction surfaces were established by passing circular arcs through the point of maximum thickness and tangent to 0.010-inch radius circles forming the leading and trailing edges. The blade sections were stacked so that their centers of gravity formed a radial line passing through the rotor axis, as previously noted. Blade nomenclature is defined in figure 4.

Blade mean line camber angles were computed from the equation

$$\varphi^0 = \Delta\beta' - i + \delta$$

Incidence and deviation angles were found using the method of reference 2 with the following exception. The correction factor $(i_P - i_{2\text{-}D})$ in the equation

$$i_P = (i_{2\text{-}D}) + (i_P - i_{2\text{-}D})$$

was chosen on the basis of data from reference 3. A chord of 1.49 inches at all radii was selected to give an integral number of blades for the desired solidity

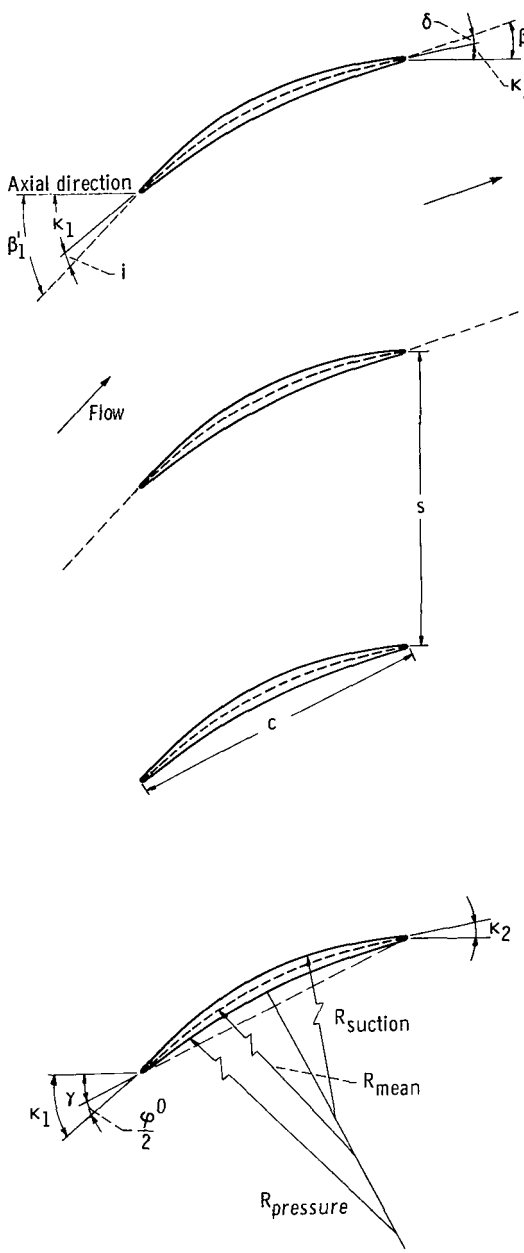

Figure 4. - Blade nomenclature.

TABLE II. - BLADE DESIGN VALUES

[Number of blades, 19; radial tip clearance, 0.016 in.; leading- and trailing-edge radii, 0.010 = constant.]

Radius ratio, r/r_t	Incidence angle, i, deg	Deviation angle, δ, deg	Camber angle, φ^0, deg	Solidity, σ	Setting angle, γ, deg	Ratio of maximum thickness to chord, t_{max}/c
1.00	-3.5	7.5	27.0	1.00	55.0	0.070
.95	-4.8	11.0	35.8	1.05	50.7	.075
.90	-5.1	13.7	42.7	1.11	46.2	.080
.85	-3.4	13.8	42.6	1.18	43.3	.085
.80	-1.7	15.0	43.4	1.25	39.8	.090

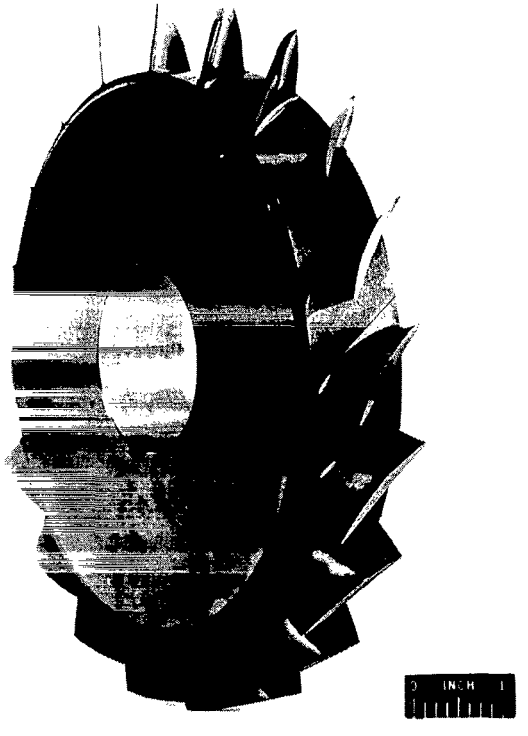

C-65-2020

Figure 5. - Rotor.

of 1.0 at the tip. No exact rule was used to select this value of solidity. However, some unpublished data from a 5-inch diameter, 0.7 hub-tip rotor, with blade loadings similar to those of the rotor reported in reference 3 but with a blade tip solidity of 1.5, did indicate increased losses at all elements.

Blade maximum thickness to chord ratio t_{max}/c values at the hub and tip sections and the linear distribution with radius were both arbitrarily assigned. Stress levels at various blade sections were then checked to ensure mechanical integrity. Radial distributions of significant blade design parameters are listed in table II. The assembled rotor is shown in figure 5.

APPARATUS AND PROCEDURE

Test Facility

The rotor was tested in the Lewis water tunnel which was described in reference 5. A schematic diagram of the test loop is shown

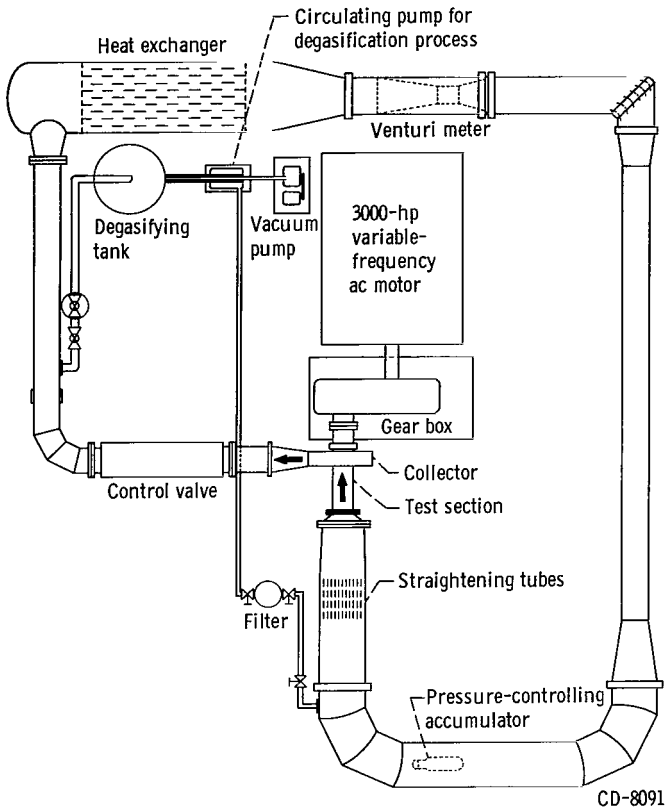

Figure 6. - Schematic of test loop.

in figure 6. Before testing, the water in the loop was conditioned by reducing gas content to approximately 1 part per million by weight and by circulating the water through a filter capable of removing solid particles larger than 5 microns. During the test, gas content was maintained less than 3 parts per million by weight.

Test Procedure and Instrumentation

A noncavitating characteristic curve was taken by holding net positive suction head and tip speed constant while varying the flow. The passage was surveyed radially and measurements of total pressure, static pressure, and flow angle were recorded at approximately 5, 10, 20, 30, 50, 70, and 90 percent of the passage height from the blade tip. A total and a static pressure probe (fig. 7) were located approximately 1 inch ahead of the rotor and 5/8 inch behind the rotor. The probes were automatically alined with the flow direction by means of a null balance system. A head correction factor for the static probes was determined in an air tunnel and applied to the results recorded in the water tunnel. Overall loop instrumentation used included a venturi meter, a water temperature measurement and control system, a speed pickup with electronic counter, and an inlet pressure transducer.

Cavitating characteristic curves were taken at several net positive suction heads with the survey probes set at the 10 percent measuring station where the effect of cavitation on head rise was expected to appear first. Also, complete radial surveys were taken at four cavitating H_{sv} with the flow held constant at approximately the design value. Cavitation in the rotor was observed visually using a movie camera and synchronized light source.

Performance of this rotor in the stall region was investigated by recording venturi flow and rotor head rise with the survey probes at the 50 percent measuring station.

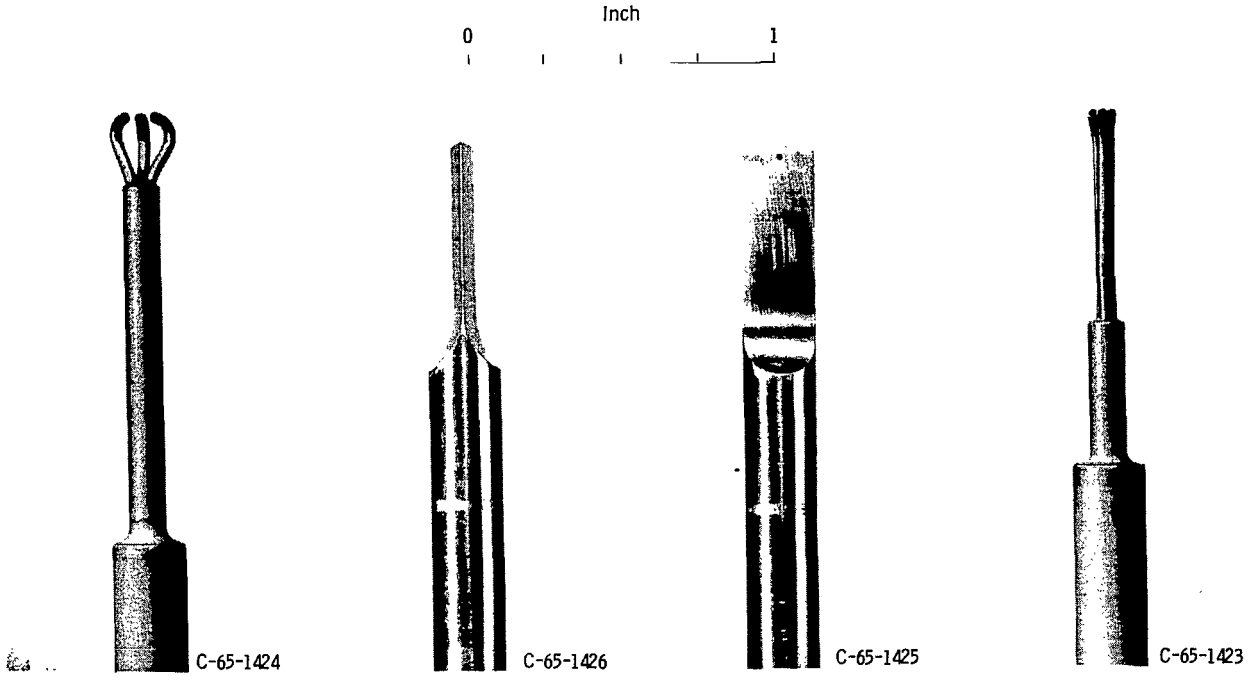

(a) Total-pressure claw. (b) Static-pressure wedge. (c) Total-pressure cobra.

Figure 7. - Probes.

Midpassage head rise was recorded over a range of flows at a reduced tip speed for a noncavitating H_{sv}. High-frequency-response pressure transducers were located in the casing at the inlet and outlet measuring stations to detect pressure fluctuations. The output signals from the high-frequency-response transducers were recorded by an oscillograph. The signal could also be displayed on an oscilloscope.

The estimated inherent accuracies of measuring and recording systems were:

Flow rate, Q, percent of design flow	±1.0
Rotative speed, N, percent	±0.5
Rotor head rise, ΔH, percent at design flow	±1.0
Velocity head, $V^2/2g_c$, percent at design flow	$<\pm 1.5$
Flow angle, β, deg	±1.0

Inaccuracies in the data due to circumferential variations, secondary flows, etc. could not be evaluated. Integrated weight flow errors shown in figure 8 gave an indication of the accuracy of measuring with the survey instruments. The level of accuracy reflected by figure 8 was considered to be reasonably good.

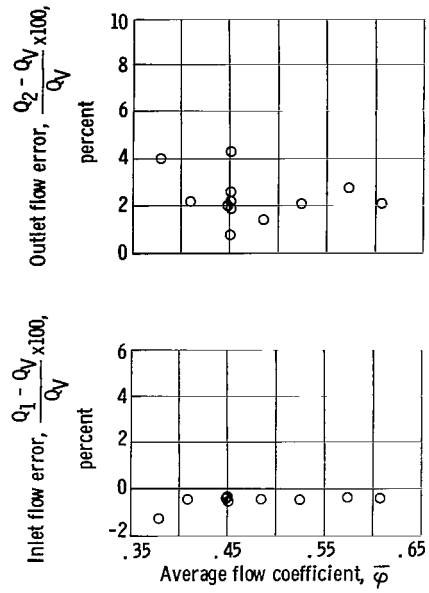

Figure 8. - Comparison of integrated flows at blade inlet and outlet with those measured by venturi meter.

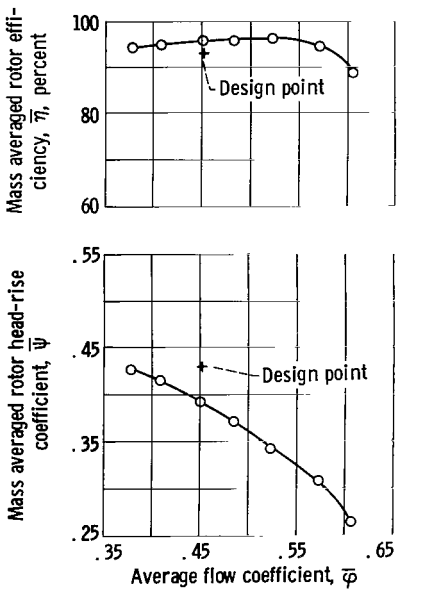

Figure 9. - Overall performance of axial-flow-pump rotor for noncavitating conditions. Rotor tip speed, 118 feet per second.

RESULTS AND DISCUSSION

Noncavitating and cavitating results are presented in separate sections. The noncavitating net positive suction head H_{sv} was selected by first determining the H_{sv} (for a given speed and maximum flow) above which no increase in head rise could be measured. Noncavitating H_{sv} was set as much above this value as strength considerations of the collector would allow.

In order to determine the extent of the casing boundary layer at the inlet to this rotor, velocity profiles across the boundary layer on the outer wall casing were measured for several values of flow coefficient. These velocity profiles were measured with survey instrumentation rather than special probes. These measurements indicated:

(1) The blade element 5 percent of the passage height from the outside wall lay inside the boundary layer. The blade element 10 percent of the passage height from the wall lay in the region where the boundary layer and the free stream coalesced. Data at this latter station can be considered for describing blade-element performance.

(2) Integration of the profiles to obtain a displacement thickness on the tip casing and the assumption of an equal displacement thickness on the long stationary inlet hub casing led to an inlet casing boundary layer blockage factor of approximately 3 percent of the annulus area. Since the annular wall boundary layers reduce the effective flow area, the inlet velocity diagrams were reached at a $\overline{\varphi}$ lower than the design φ_i. For comparison with design, performance and flow conditions at a measured overall flow coefficient of $\overline{\varphi} = 0.97\ \varphi_i = (0.97)(0.466) = 0.452$ were used.

Noncavitating Performance

Overall performance. - The noncavitating overall performance curves are shown in figure 9. The symbol $\overline{\psi}$ represents a mass averaged rotor-head-rise coeffi-

cient. The average flow coefficient $\overline{\varphi}$ is based on venturi measured flow, inlet geometric area, and blade-tip speed as defined by equation (C7) in appendix C.

The characteristic curve was limited at low flows by unstable flow conditions evidenced by large rig vibrations and noise, and at high flows by the pressure-loss characteristics of the test loop.

At $\overline{\varphi} = 0.452$ a $\overline{\psi}$ of 0.391 was reached as compared with the design value of 0.427. The mass-averaged efficiency $\overline{\eta}$ computed from test results was 95.5 percent at $\overline{\varphi} = 0.452$ while 92.8 percent was computed from design parameter values. These comparisons indicate that the desired energy addition was not achieved. The data in figure 9 also show that the efficiency remained high over a large portion of the flow range.

Radial distributions. - Survey measurements of total head, flow angle, and velocity head are shown in figure 10 as radial distributions of inlet total head, inlet and outlet flow angle, inlet and outlet flow coefficient and rotor head-rise coefficient for four flows

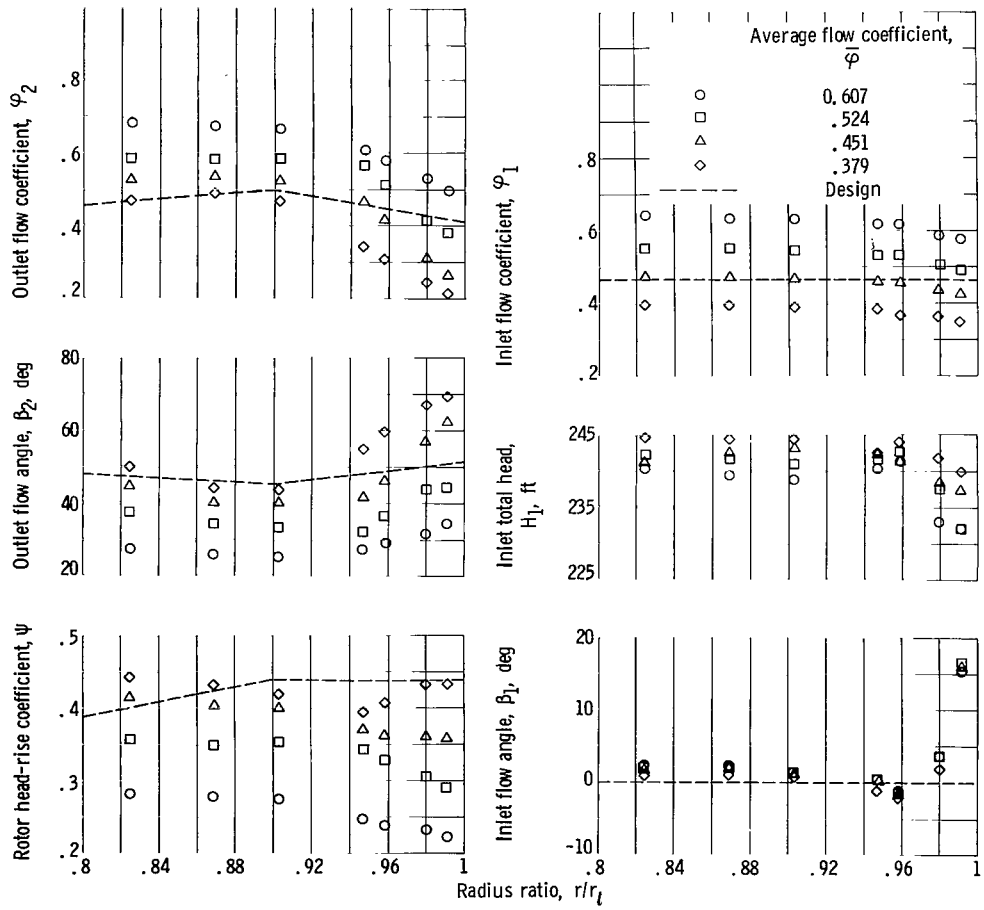

Figure 10. - Radial distributions of flow and performance parameters for noncavitating conditions. Rotor tip speed, 118 feet per second.

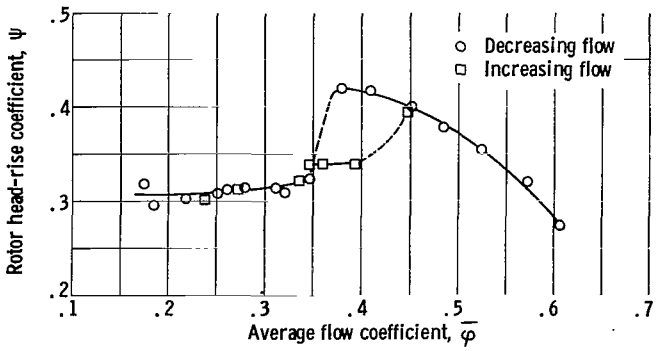

Figure 11. - Performance of axial-flow-pump rotor at midpassage for noncavitating conditions. Rotor tip speed, 78 feet per second.

covering the range of operations. These parameters are presented to be compared with design values and to be used to compute velocity diagrams if desired.

Examination of figure 10 shows that the inlet flow coefficient is nearly constant except near the tip. The design assumption of constant inlet velocity appears to be justified. The inlet total head falls off at the tip because of boundary layer effects. The measured inlet fluid angle was within $2\frac{1}{2}^{\circ}$ of the axial direction except at the 5 and 10 percent stations. The local head-rise coefficient for approximately design flow is lower than the design distribution except at the hub. This difference probably resulted from a lower-than-required energy addition. No attempt was made herein to analyze blade-element data.

Stall Performance

Figure 11 shows the variation of rotor head-rise coefficient ψ measured across the midpassage station as flow was reduced into the stalled operating range. This portion of the investigation was carried out at a reduced speed (U_t = 78 ft/sec). As $\overline{\varphi}$ was reduced from a maximum value, ψ increased consistently to a maximum value of 0.425 at $\overline{\varphi}$ of 0.38. As $\overline{\varphi}$ was further decreased, the rotor stalled and ψ dropped off very rapidly

TABLE III. - SUMMARY OF HIGH FREQUENCY RESPONSE TRANSDUCER DATA

[Rotor tip speed, U_t = 78 ft/sec.]

Parameters	Units	Unstalled conditions		Unstable operating range			
		$\overline{\varphi} > 0.38$		$0.14 < \overline{\varphi} < 0.22$		$0.25 < \overline{\varphi} < 0.35$	
		Inlet	Outlet	Inlet	Outlet	Inlet	Outlet
h_{pp}	ft	~2	~7	~45	~28	~65	~28
f	cps	Not well defined		40 to 43	40 to 43	20	20
ΔH	ft	52 to 80		~59	~59	~59	~59
h_1	ft	125	125	125	125	125	125

to a value approximately 75 percent of the maximum value and remained at about this level. Also, at the flow where ψ fell off, abrupt large increases in vibrations and noise level were noted.

Static pressure fluctuations at the blade inlet and outlet measuring stations were detected by means of high-frequency-response transducers mounted in the outer wall casing. The results of this portion of the investigation are summarized in table III. At the blade inlet, static pressure fluctuations with peak-to-peak amplitudes of 45 to 65 feet were observed in the stalled range. The head rise across the rotor in this stalled condition was approximately constant at 59 feet. The amplitude of 45 to 65 feet represented an increase of approximately 20 to 30 times over amplitudes measured in the stable operating region. In this stalled region pressure fluctuations seemed to primarily occur at frequencies of approximately 20 and 40 cycles per second. A frequency spectrum analysis of this data had not been conducted.

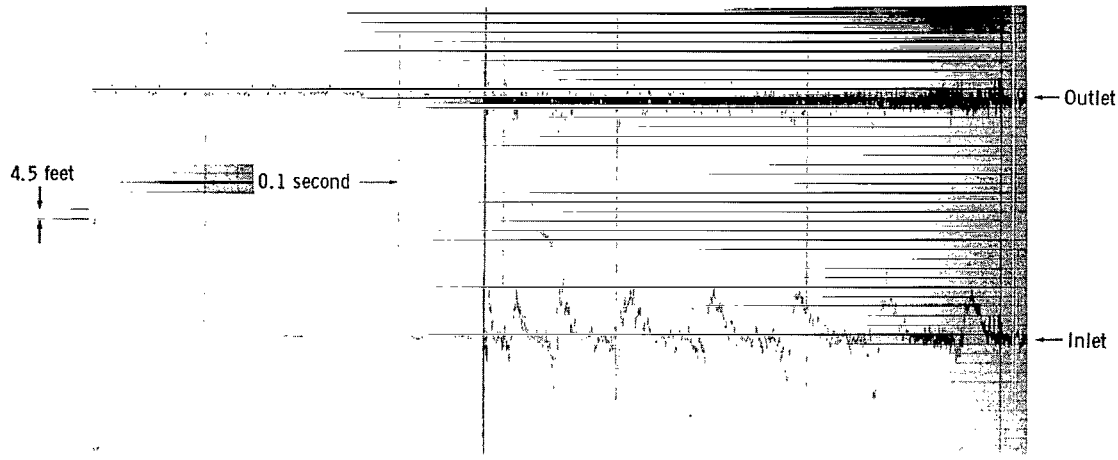

(a) Stalled and unstalled conditions with average flow coefficient about 0.38.

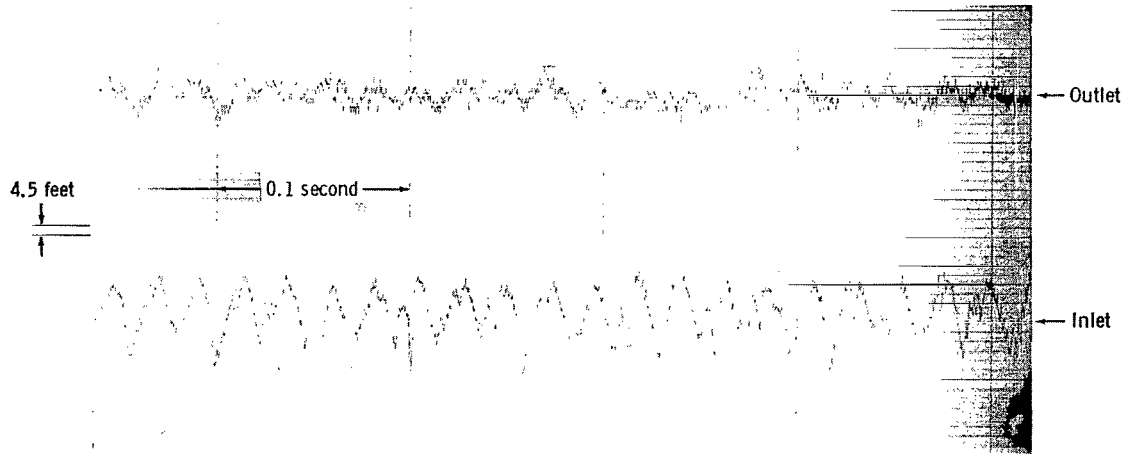

(b) Stalled conditions with average flow coefficient about 0.14.

Figure 12. - High-frequency response pressure traces.

At the blade outlet, peak-to-peak amplitudes in the stalled operating range were approximately four times as large as those measured in the unstalled range. The 20 and 40 cycles per second frequencies were also detected at the outlet in the stalled region. Typical traces of pressure fluctuations recorded at the inlet and outlet of the blade as flow was decreased from the stable operating range into the stalled region are shown in figure 12.

As flow was increased while in a stalled condition, stable flow conditions were not again established until a $\overline{\varphi}$ of approximately 0.45 was attained. Thus, a hysteresis loop was formed as shown in figure 11 (p. 12). Any minute increase in flow from the operating point $\overline{\varphi} = 0.395$, $\psi = 0.34$ on the stalled characteristic resulted in the reestablishment of unstalled flow conditions. The dashed line through this point to some operating point on the unstalled characteristic then essentially represents a system operating characteristic and could be expected to vary with each system in which the pump is installed. In the system used in this investigation the design-flow operating point lies on the hysteresis loop. When this occurs, some problems in attaining design flow during startup and acceleration and recovering from a stalled condition might be anticipated.

Cavitation Performance

A small amount of cavitation data was obtained for this highly loaded rotor to determine the H_{SV} requirement of such a main stage rotor. At approximately design flow, four complete passage surveys were taken at H_{SV} ranging from 239 to 104 feet ($\overline{k} = 0.76$ to $\overline{k} = 0.23$, respectively). The overall performance results of this portion of the investigation are presented in figure 13 which shows $\overline{\psi}$ (mass-averaged head coefficient) as a function of H_{SV} for $\overline{\varphi} \approx 0.451$ = constant. The data of the figure indicate that $\overline{\psi}$ remains constant as H_{SV} is lowered until a value of approximately 145 feet ($\overline{k} = 0.40$) is reached, where $\overline{\psi}$ first increases and then decreases as H_{SV} is further reduced.

Visual studies were also made at approximately design $\overline{\varphi}$ for the same range of H_{SV}. Figure 14 shows photographs of the cavitation present at four values of H_{SV}. Note that the photographs of figure 14 may be related to the performance curve shown in figure 13 since the same range of H_{SV} is presented in both figures. The flow conditions at H_{SV} = 326 feet ($\overline{k} = 1.08$), the H_{SV} at which tip vortex cavitation was first detected visually are shown in figure 14(a). The inception of blade surface streamers which formed well back from the leading edge of the blade occurred at a H_{SV} of 139 feet ($\overline{k} = 0.36$). The flow conditions at H_{SV} = 139 feet are shown in figure 14(b). As shown in figure 13 $\overline{\psi}$ was increasing at this H_{SV}. The

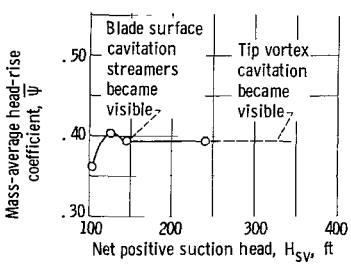

Figure 13. - Axial-flow-pump performance as function of net positive suction head. Rotor tip speed, 118 feet per second; average flow coefficient, 0.451.

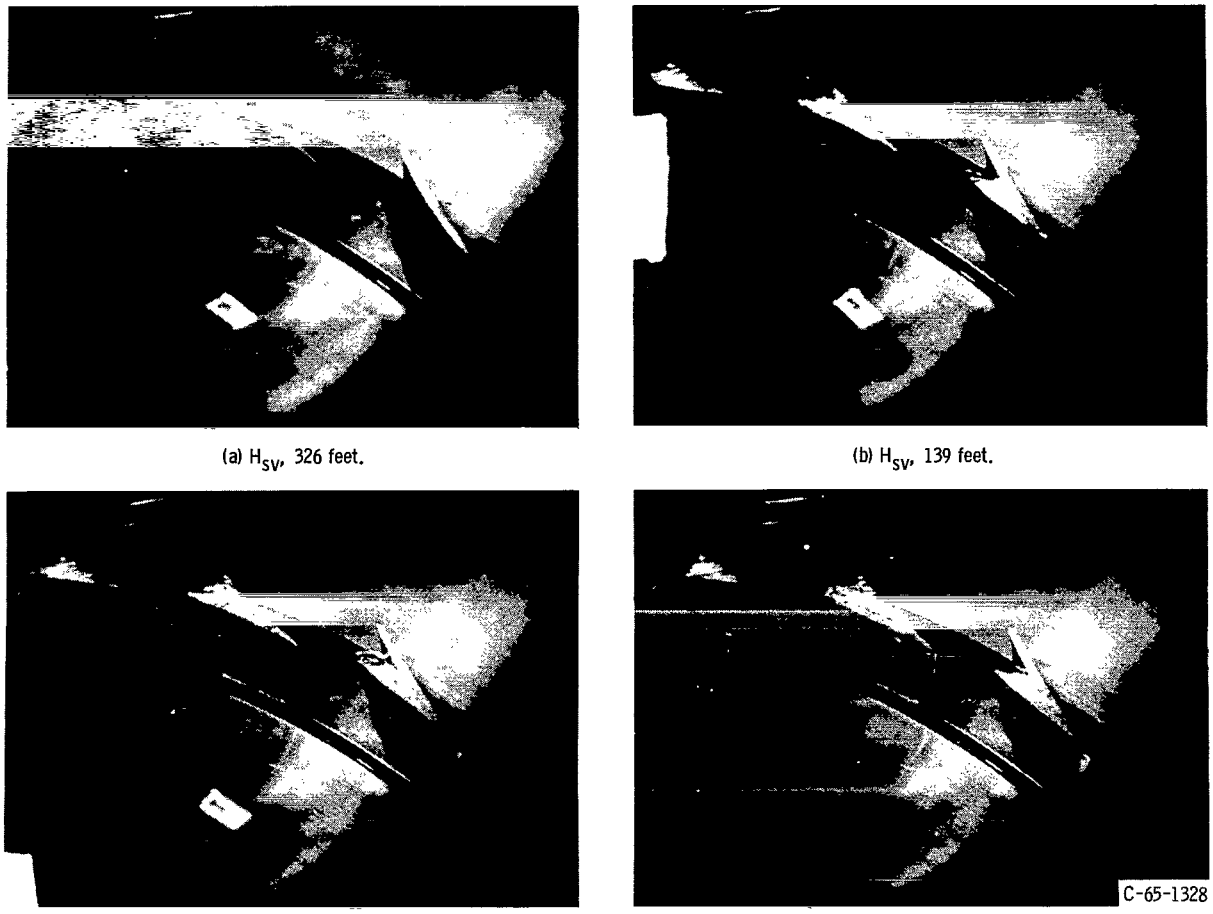

(a) H_{sv}, 326 feet.

(b) H_{sv}, 139 feet.

(c) H_{sv}, 124 feet.

(d) H_{sv}, 101 feet.

Figure 14. - Cavitation present at four net positive suction heads for design flow.

buildup of cavitation as H_{sv} was further reduced is illustrated in figures 14(c) and (d).

Radial distributions shown in figure 15 indicate the effects of cavitation on selected parameters at the inlet and outlet of the blade for approximately design flow. The inlet flow angle and flow-coefficient distributions shown in the figure do not vary substantially with decreasing H_{sv}. The local head-rise coefficient for $H_{sv} = 127$ feet ($\bar{k} = 0.32$) showed an increase over noncavitating values across the upper half of the blade. This increase in ψ was reflected by the increase in $\bar{\psi}$ shown in figure 13 at a $H_{sv} = 127$ feet. As H_{sv} was reduced to 104 feet ($\bar{k} = 0.23$), ψ values below noncavitating values were measured at all radii, as shown in figure 15, with the largest difference at the center of the blade. Figure 13 shows a corresponding decrease in $\bar{\psi}$ for $H_{sv} = 104$ feet.

The cavitation performance presented so far was all taken at approximately design flow. Additional characteristic performance curves are presented in figure 16 showing the variation of ψ_{10} (measured with the survey probes set at the 10 percent data station) over the range of flows for five values of H_{sv}. One of the five H_{sv} is a noncavitating

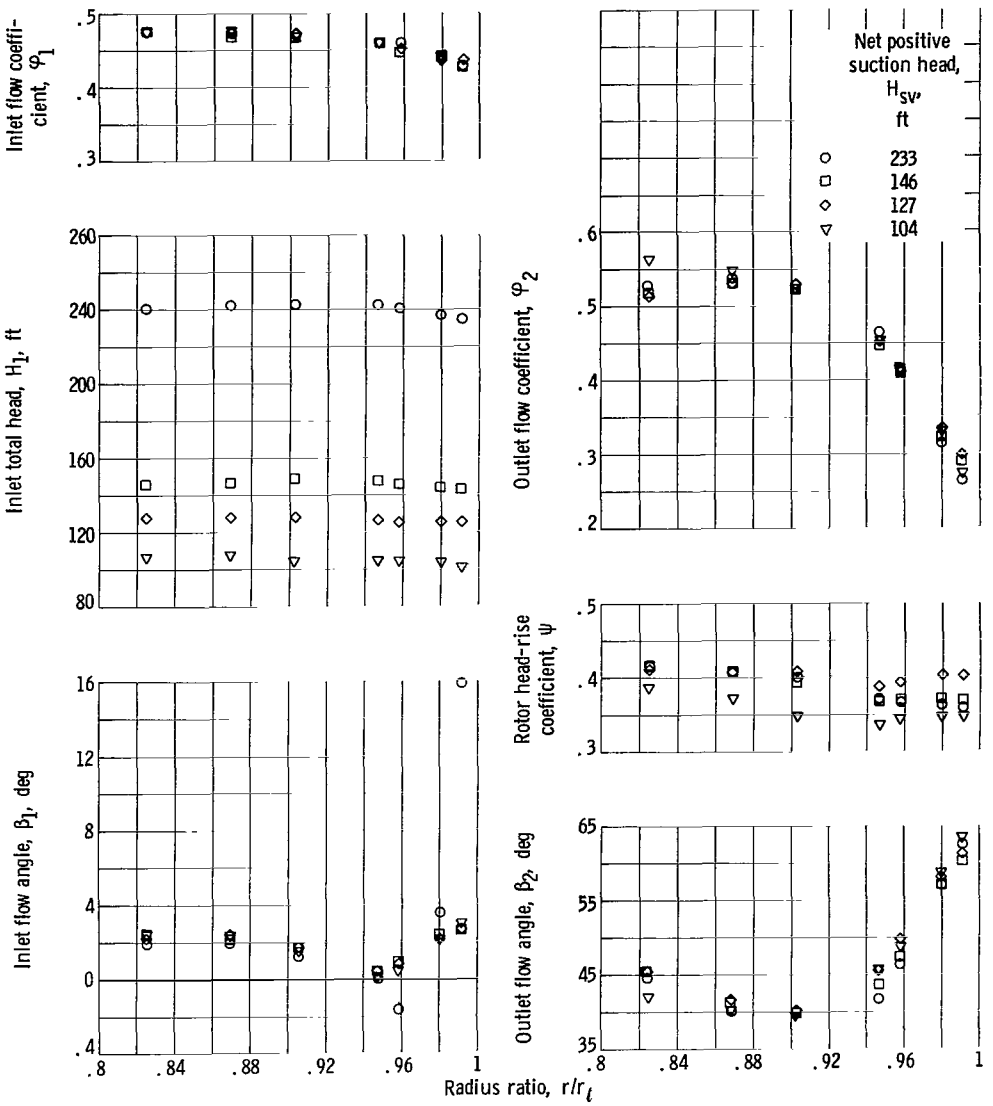

Figure 15. - Radial distributions of flow and performance parameters for cavitating conditions. Rotor tip speed, 118 feet per second. Average flow coefficient, 0.45.

value to provide a basis for comparison.

When the H_{sv} was lowered to 193 feet ($\bar{k} = 0.57$) a reduction of ψ_{10} from the noncavitating values was observed in the high flow region. As the H_{sv} was further lowered the reduction in ψ_{10} increased in magnitude and occurred over increasing portions of the flow range. For $H_{sv} = 104$ feet ($\bar{k} = 0.23$) the decrease in ψ_{10} due to cavitation occurred over the complete flow range.

Note that for all $\overline{\varphi} < 0.53$ there was a H_{sv} for which the ψ_{10} shown in figure 16 was larger than the corresponding noncavitating value. This indicates that a rise in $\overline{\psi}$, similar to that shown in figure 13, probably occurred for all $\overline{\varphi} < 0.53$. The data shown

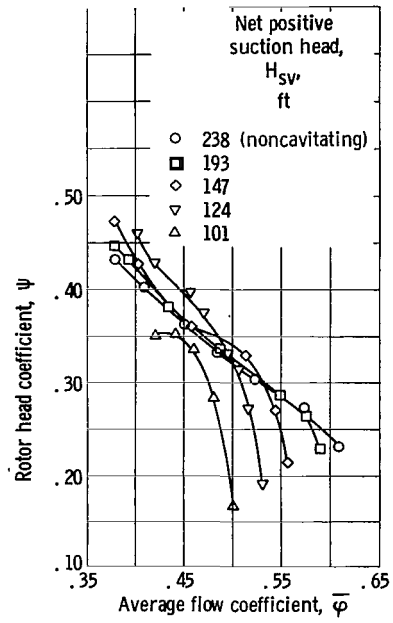

Figure 16. - Characteristic performance curves of axial-flow-pump rotor at 10 percent of passage height for cavitating conditions. Rotor tip speed, 118 feet per second.

in figure 16 indicates that the increase in ψ_{10} over noncavitating values became larger as $\overline{\varphi}$ was reduced.

SUMMARY OF RESULTS

A 9-inch diameter axial-flow pump rotor with an 0.8 hub-tip radius ratio and a blade-tip diffusion factor of 0.66 was designed by blade-element techniques and tested in water. The measured performance levels and unstalled operating range indicate that designs with this magnitude of flow coefficient and blade loading can be considered for staging in high-pressure, axial-flow pumps. Significant results are as follows:

1. With the level of loading used in design, a relatively high flow coefficient and a radial distribution of energy addition increasing from hub to tip were required to obtain a head-rise coefficient approximately constant radially and a gradient of outlet flow coefficient which was considered acceptable. A flow coefficient of 0.466 was selected.

2. At design flow, the rotor produced an overall head-rise coefficient of 0.391 as compared to the design value of 0.427. Design efficiency was 92.8 percent while an overall efficiency of 95.5 percent was achieved experimentally.

3. As flow was reduced from the maximum value, the rotor operated in a stalled

condition at flow coefficients below $\overline{\varphi} = 0.380$ (compared with the design flow coefficient of 0.452). Pressure fluctuations increased significantly at both the blade inlet and outlet when the flow became unstable. Frequencies of the pressure fluctuations in the stalled region were well defined at the blade inlet but not at the blade outlet. When flow was increased from a stalled operating point, a hysteresis loop was indicated.

4. At design flow, a decrease in head-rise coefficient due to cavitation occurred at $H_{sv} = 115$ feet ($\bar{k} = 0.27$). As H_{sv} was decreased from a noncavitating value, for $0.38 < \overline{\varphi} < 0.54$, a slight improvement in head rise was indicated just prior to a fall-off in performance. Radial distributions of flow and performance indicated this increase in ψ occurred primarily in the blade tip region.

Lewis Research Center,
National Aeronautics and Space Administration,
Cleveland, Ohio, June 16, 1965.

APPENDIX A

SYMBOLS

A	area
c	blade chord, in.
D	blade diffusion factor, eq. (B12)
f	frequency, cps
g_c	standard acceleration of gravity, $32.174 \frac{lb_m\ ft}{lb_f\ sec^2}$
H	total head, ft
ΔH	blade-element head rise, ft, eq. (C1)
H_{sv}	net positive suction head, ft, eq. (C9)
h	static head, ft
h_v	vapor pressure, ft
i	incidence angle, angle between inlet flow direction and tangent to blade mean camber line at leading edge, deg (see fig. 4)
$\bar{k}$	blade cavitation number, eq. (C8)
N	rotative speed, rpm
Q	flow rate, gal/min
r	radius, ft
t	blade thickness, in.
U	rotor tangential velocity, ft/sec
V	absolute velocity, ft/sec
β	flow angle with respect to axial direction, deg
γ	blade setting angle, angle between blade chord and axial direction, deg (see fig. 4)
δ	deviation angle, angle between outlet flow direction and the tangent to the blade camber line at trailing edge, deg (see fig. 4)
η	rotor efficiency, percent, eq. (C3)
κ	blade angle, angle between the tangent to the blade camber line and axial direction, deg (see fig. 4)
σ	blade solidity, ratio of blade chord to blade tangential spacing
φ	flow coefficient, eq. (C2)
φ^0	blade camber angle, deg (see fig. 4)
ψ	rotor head-rise coefficient, eq. (B19)
$\bar{\omega}$	rotor relative total head-loss coefficient, eq. (B14)

Subscripts:

h	hub
i	ideal
max	maximum
P	pump

pp	peak-to-peak
r	radial position
t	tip
V	measured with venturi meter
z	axial component
θ	tangential component
1	rotor inlet
2	rotor outlet
2-D	low-speed two-dimensional cascade
10	measured at the 10 percent station

Superscripts:

$\bar{}$	averaged quantity
'	relative

APPENDIX B

BLADE ELEMENT EQUATIONS FOR DESIGN CALCULATION PROCEDURE

Inlet relative fluid angle (for $V_{\theta,1} = 0$)

$$\beta_1' = \cot^{-1}\left(\frac{\varphi_1}{\frac{r}{r_t}}\right) \tag{B1}$$

Ratio of inlet relative velocity to tip speed

$$\frac{V_1'}{U_t} = \frac{\varphi_1}{\cos \beta_1'} \tag{B2}$$

Ideal head rise

$$\Delta H_i = \frac{U_2 V_{\theta,2} - U_1 V_{\theta,1}}{g_c} \tag{B3}$$

or, for $V_{\theta,1} = 0$

$$\Delta H_i = \frac{U_2 V_{\theta,2}}{g_c} \tag{B4}$$

Ideal head-rise coefficient

$$\psi_i = \frac{g_c \Delta H_i}{U_t^2} \tag{B5}$$

Radial distribution of ideal head rise coefficient

$$\psi_i = 0.508 \frac{r}{r_t} - 0.0036 \qquad 0.8 \leq \frac{r}{r_t} \leq 0.9 \tag{B6}$$

$$\psi_i = 0.690 \frac{r}{r_t} - 0.1674 \qquad 0.9 \leq \frac{r}{r_t} \leq 1.0 \tag{B7}$$

Ratio of outlet tangential velocity to tip speed (for $V_{\theta,1} = 0$)

$$\frac{V_{\theta,2}}{U_t} = \frac{\psi_i}{\frac{r}{r_t}} \tag{B8}$$

Ratio of outlet relative tangential velocity to tip speed

$$\frac{V'_{\theta,2}}{U_t} = \frac{r}{r_t} - \frac{V_{\theta,2}}{U_t} \tag{B9}$$

Outlet relative fluid angle

$$\beta'_2 = \cot^{-1} \frac{\varphi_2}{\frac{V'_{\theta,2}}{U_t}} \tag{B10}$$

Ratio of outlet relative velocity to tip speed

$$\frac{V'_2}{U_t} = \frac{\varphi_2}{\cos \beta'_2} \tag{B11}$$

Blade diffusion factor

$$D = 1 - \frac{V'_2}{V'_1} + \frac{r_2 V_{\theta,2} - r_1 V_{\theta,1}}{\sigma V'_1 (r_1 + r_2)} \tag{B12}$$

or, for $r_1 = r_2$

$$D = 1 - \frac{V_2}{V'_1} + \frac{\Delta V_\theta}{2\sigma V'_1} \tag{B13}$$

Rotor relative total head-loss coefficient

$$\overline{\omega} = \frac{H'_{2,i} - H'_2}{\frac{V'^2_1}{2g_c}} = \frac{\Delta H_i - \Delta H}{\frac{V'^2_1}{2g_c}} \tag{B14}$$

Radial equilibrium

$$\frac{dh}{d\frac{r}{r_t}} = \frac{V_\theta^2}{g_c \frac{r}{r_t}} \tag{B15}$$

Outlet local static pressure

$$h_{2,r} = H_{1,r} + \Delta H_r - \frac{V^2_{\theta,2r}}{2g_c} - \frac{V^2_{z,2r}}{2g_c} \tag{B16}$$

Outlet local flow coefficient using (B6) or (B7) and (B15)

$$(\varphi_{2,r+1})^2 = (\varphi_{2,r})^2 + 2(\psi_{r+1} - \psi_r) - \frac{0.005458}{\frac{r_{r+1}}{r_t}} + \frac{0.005458}{\frac{r_r}{r_t}}$$

$$+ 0.2581 \ln\left(\frac{\frac{r_r}{r_t}}{\frac{r_{r+1}}{r_t}}\right) \qquad 0.8 \le \frac{r}{r_t} \le 0.9 \tag{B17}$$

$$(\varphi_{2,r+1})^2 = (\varphi_{2,r})^2 + 2(\psi_{r+1} - \psi_r) - \frac{0.2310}{\frac{r_{r+1}}{r_t}} + \frac{0.2310}{\frac{r_r}{r_t}}$$

$$+ 0.4761 \ln\left(\frac{\frac{r_r}{r_t}}{\frac{r_{r+1}}{r_t}}\right) \qquad 0.9 \leq \frac{r}{r_t} \leq 1.0 \qquad \text{(B18)}$$

Head-rise coefficient

$$\psi = \frac{g_c \Delta H}{U_t^2} = \psi_i - \frac{\overline{\omega}}{2}\left(\frac{V_i'}{U_t}\right)^2 \qquad \text{(B19)}$$

Average outlet flow coefficient

$$\overline{\varphi}_2 = \frac{\sum_{r=1}^{4}\left(\varphi_{2,r}\frac{r_r}{r_t} + \varphi_{2,r+1}\frac{r_{r+1}}{r_t}\right)\left(\frac{r_r}{r_t} - \frac{r_{r+1}}{r_t}\right)}{\sum_{r=1}^{4}\left(\frac{r_r}{r_t} + \frac{r_{r+1}}{r_t}\right)\left(\frac{r_r}{r_t} - \frac{r_{r+1}}{r_t}\right)} \qquad \text{(B20)}$$

APPENDIX C

BLADE-ELEMENT EQUATIONS

Blade-element head rise

$$\Delta H = H_2 - H_1 \tag{C1}$$

Flow coefficient

$$\varphi = \frac{V_z}{U_\ell} \tag{C2}$$

Efficiency

$$\eta = \frac{\Delta H}{\Delta H_i} \times 100 \tag{C3}$$

OVERALL AND AVERAGED PARAMETER EQUATIONS

Mass-averaged head rise

$$\overline{\Delta H} = \frac{\sum_{r=1}^{6} (r_r V_{z,r} \Delta H_r + r_{r+1} V_{z,r+1} \Delta H_{r+1})(r_r - r_{r+1})}{\sum_{r=1}^{6} (r_r V_{z,r} + r_{r+1} V_{z,r+1})(r_r - r_{r+1})} \tag{C4}$$

Mass-averaged ideal head rise

$$\overline{\Delta H}_i = \frac{1}{g_c} \left(\overline{U_2 V_{2,\theta}} - \overline{U_1 V_{1,\theta}} \right)$$

for $V_{1,\theta} = 0$

$$\Delta\overline{H}_i = \frac{1}{g_c}\left(\overline{U_2 V_{2,\theta}}\right) = \frac{1}{g_c}\left(\frac{\sum_{r=1}^{6} U_{2,r} V_{2,\theta,r} A_{2,r} V_{2,z,r}}{\sum_{r=1}^{6} A_{2,r} V_{2,z,r}}\right)$$

Mass-averaged efficiency

$$\overline{\eta} = \frac{\Delta\overline{H}}{\Delta\overline{H}_i} \times 100 \tag{C5}$$

Mass-averaged head-rise coefficient

$$\overline{\psi} = \frac{g_c \Delta\overline{H}}{U^2} \tag{C6}$$

Average flow coefficient

$$\overline{\varphi} = \frac{Q_V}{448.8\,\pi\left(r_t^2 - r_h^2\right)U_t} \tag{C7}$$

Blade cavitation number

$$\overline{k} = \frac{2g_c H_{sv}}{U_t^2\left(1 + \overline{\varphi}^2\right)} - \frac{\overline{\varphi}^2}{\left(1 + \overline{\varphi}^2\right)} \tag{C8}$$

Net positive suction head

$$H_{sv} = H_1 - h_v \tag{C9}$$

REFERENCES

1. Lieblein, Seymour; Schwenk, Francis C.; and Broderick, Robert L.: Diffusion Factor for Estimating Losses and Limiting Blade Loadings in Axial-Flow-Compressor Blade Elements. NACA RM E53DO1, 1953.

2. Robbins, William H.; Jackson, Robert J.; and Lieblein, Seymour: Blade-Element Flow in Annular Cascades. Aerodynamic Design of Axial-Flow Compressors (Revised), ch. VII, NASA SP-36, 1965, pp. 227-254. (Supersedes NACA RM's E56BO3, E56BO3a, and E56BO3b.)

3. Crouse, James E.; and Sandercock, Donald M.: Blade-Element Performance of 0.7 Hub-Tip Radius Ratio Axial-Flow-Pump Rotor with Tip Diffusion Factor of 0.43. NASA TN D-2481, 1964.

4. Crouse, James E.; and Sandercock, Donald M.: Design and Overall Performance of an Axial-Flow-Pump Rotor with a Blade Tip Diffusion Factor of 0.43. NASA TN D-2295, 1964.

5. Crouse, James E.; Montgomery, John C.; and Soltis, Richard F.: Investigation of the Performance of an Axial-Flow-Pump Stage Designed by the Blade-Element-Theory - Design and Overall Performance. NASA TN D-591, 1961.

"The aeronautical and space activities of the United States shall be conducted so as to contribute . . . to the expansion of human knowledge of phenomena in the atmosphere and space. The Administration shall provide for the widest practicable and appropriate dissemination of information concerning its activities and the results thereof."

—NATIONAL AERONAUTICS AND SPACE ACT OF 1958

NASA SCIENTIFIC AND TECHNICAL PUBLICATIONS

TECHNICAL REPORTS: Scientific and technical information considered important, complete, and a lasting contribution to existing knowledge.

TECHNICAL NOTES: Information less broad in scope but nevertheless of importance as a contribution to existing knowledge.

TECHNICAL MEMORANDUMS: Information receiving limited distribution because of preliminary data, security classification, or other reasons.

CONTRACTOR REPORTS: Technical information generated in connection with a NASA contract or grant and released under NASA auspices.

TECHNICAL TRANSLATIONS: Information published in a foreign language considered to merit NASA distribution in English.

TECHNICAL REPRINTS: Information derived from NASA activities and initially published in the form of journal articles.

SPECIAL PUBLICATIONS: Information derived from or of value to NASA activities but not necessarily reporting the results of individual NASA-programmed scientific efforts. Publications include conference proceedings, monographs, data compilations, handbooks, sourcebooks, and special bibliographies.

Details on the availability of these publications may be obtained from:

SCIENTIFIC AND TECHNICAL INFORMATION DIVISION

NATIONAL AERONAUTICS AND SPACE ADMINISTRATION

Washington, D.C. 20546